
DIRECT-DRIVE CAPSULES FOR NIF

S. V. Weber

D. Eimerl

J. E. Rothenberg

H. E. Dalhed

M. H. Key

*C. P. Verdon**

S. M. Pollaine

Introduction

In inertial confinement fusion (ICF), large amounts of (laser) energy are delivered onto a target containing fusion fuel, usually deuterium–tritium (DT). The rocket-like blowoff of the target shell material compresses the fuel within, leading to fusion.

The direct-drive approach to ICF uses direct laser irradiation to implode the capsule. The indirect-drive approach converts laser energy to x rays in a Au hohlraum, and the x rays are used to implode the capsule. The National Ignition Facility (NIF) has been designed principally for indirect-drive ignition; however, fairly modest enhancements to the facility would make direct-drive ignition achievable as well. The facility requirements were specified in 1995 in a white paper,¹ and the design modifications necessary to meet those requirements were presented in the Advanced Conceptual Design Review.² The main requirements for direct drive are a beam configuration that is distributed nearly evenly around the capsule in all directions and a beam smoothing system in the laser front end that meets more stringent requirements than those for indirect drive. The timescale to implement these capabilities on the NIF has not yet been determined.

Background

To illuminate the capsule uniformly requires a different beam geometry than that used to drive a cylindrical hohlraum, as shown in Figure 1. For indirect drive, clusters of four beamlets are distributed in four rings, grouped in two pairs, in each hemisphere. These rings give two cones of illumination that are directed into

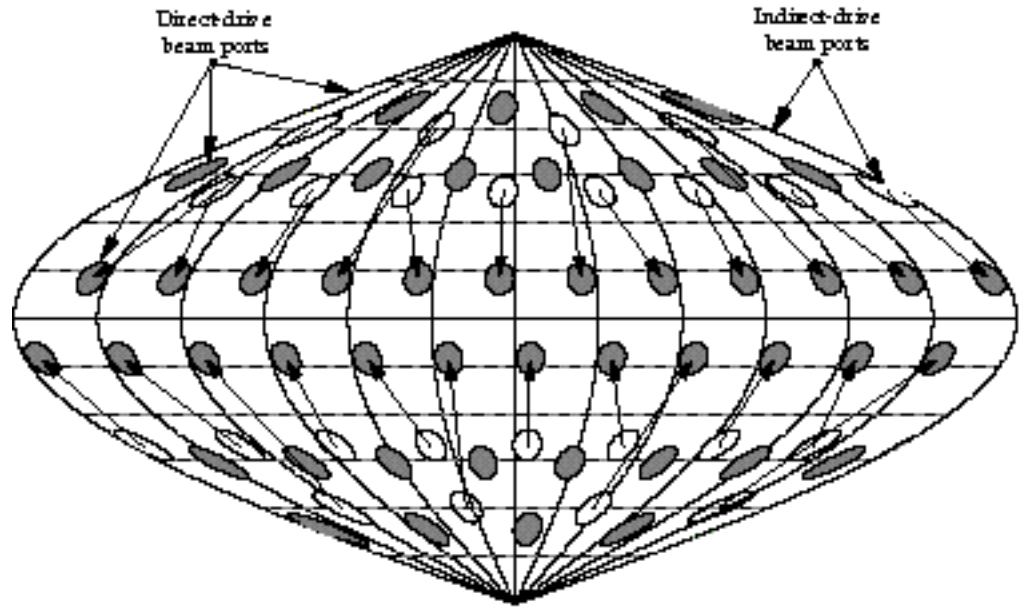
each end of a hohlraum³ at angles 23.5°, 30°, 44.5°, and 50° from the chamber axis. For direct drive, suitable illumination may be obtained by steering the beams from the second and fourth rings to a fifth ring at 77.45°, giving an intrinsic illumination uniformity (for perfect pointing and power balance) of 0.2% rms. This is considerably better than the 1% rms in spherical harmonic modes $l < 20$, which is required. However, beam pointing errors and power imbalance will also cause illumination nonuniformity. Pointing accuracy and power balance requirements, which follow from the uniformity specification, are discussed later in this article.

For indirect drive, only a fraction of the laser energy is converted into x rays, and only a fraction of the x rays are absorbed by the capsule, which makes direct drive appear to be a more efficient use of laser energy to implode a capsule. However, there are also several inefficiencies in direct drive, and, by our current understanding of target physics, it appears that about the same energy is needed to obtain ignition by either approach. Only about half of the laser energy is actually absorbed by the capsule in the direct-drive designs we have considered. The laser spot size is chosen to be comparable with the initial target diameter to get adequate illumination uniformity. As the capsule implodes, only the centers of the beams get into dense plasma and are absorbed efficiently. Also, the fraction of absorbed energy converted into implosion kinetic energy, the “rocket efficiency,” is lower for direct drive. Direct laser illumination deposits energy into lower-density plasma than indirect x-ray illumination, so a lower mass is ablated at a higher exhaust velocity, which gives a less efficient rocket.

Also, it is necessary to implode a direct-drive capsule shell on a higher adiabat than is the case for indirect drive. The adiabat characterizes the degree of degeneracy of the fuel. The usual definition of the adiabat is $\alpha = P/P_F$, where P is the pressure in the fuel, and P_F is the pressure for Fermi degenerate fuel at the same

* University of Rochester, Laboratory for Laser Energetics, Rochester, NY

FIGURE 1. Beam cluster locations on a map of the target chamber. Ports used for direct drive are shaded. Indirect-drive ports, which are not used for direct drive, are unshaded, with arrows showing how the beams are shifted to the new rings at 77.45° and 102.55° .
(20-03-0397-0432pb01)



density. Indirect-drive designs with $\alpha \approx 1$ are predicted to have adequate stability;³ direct-drive designs are predicted to need an increase of the adiabat to $\alpha \approx 2$ –4 to prevent the shell from breaking up. The higher the adiabat, the lower the fuel density for a given stagnation pressure resulting from the implosion. This lower density leads to a faster ablation rate and improved stability. However, more implosion energy is needed to achieve ignition, and the gain at a given implosion energy is lower.⁴ Lindl presents these energetics scalings in detail.⁵

The physics for the indirect-drive target design have been tested exhaustively in the work specified by the Nova Technical Contract.⁶ A significant amount of direct-drive research has also been conducted on Nova and elsewhere, but much more is required. The research program on the Omega⁷ laser at the University of Rochester, together with work at the Nike⁸ laser at the Naval Research Laboratory, the GEKKO XII⁹ laser at Osaka University, and other facilities throughout the world, will make it much more clear in a few years what the probability of success will be for direct drive as a route to ignition on the NIF.

Capsule Designs

We have examined the capsule designs (frozen DT shells surrounding DT gas) developed at the University of Rochester,¹⁰ shown in Figure 2. Practical capsules would require a thin outer layer, such as a few micrometers of CH, for mechanical support, but this layer has been omitted from our simulations. The capsules are driven with 1.5 MJ of $0.35\text{-}\mu\text{m}$ light with pulse shapes as shown in Figure 2. The capsule in Figure 2(a) uses a picket pulse shape; the one in Figure 2(b) uses a continuous pulse

shape. Both pulse shapes are used to adjust the timing of shocks through the shell to set the fuel on the desired adiabat ($\alpha = 3.7$ for the continuous pulse shape and $\alpha = 2.2$ for the picket pulse). Figure 3 shows the time history of the mass-averaged fuel adiabat. Note that most of the entropy for the continuous pulse capsule is created by the first shock, while for the picket capsule most is added by the fourth shock. The capsule yields, in 1D simulations neglecting mix, are 17 and 33 MJ for the continuous and picket designs, respectively.

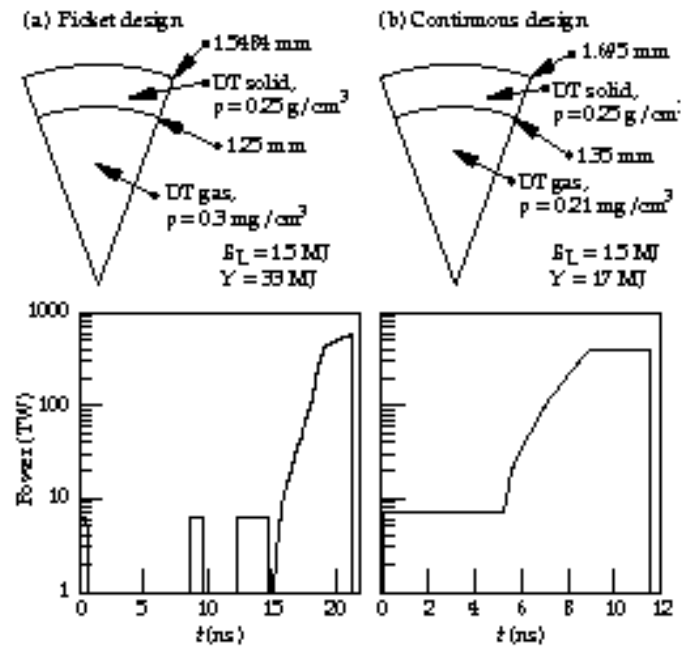


FIGURE 2. Capsule dimensions and pulse shapes for two direct-drive designs: (a) picket-pulse and (b) continuous-pulse shape. E_L is laser energy on target, and Y is fusion yield from the target.
(20-03-0397-0441pb01)

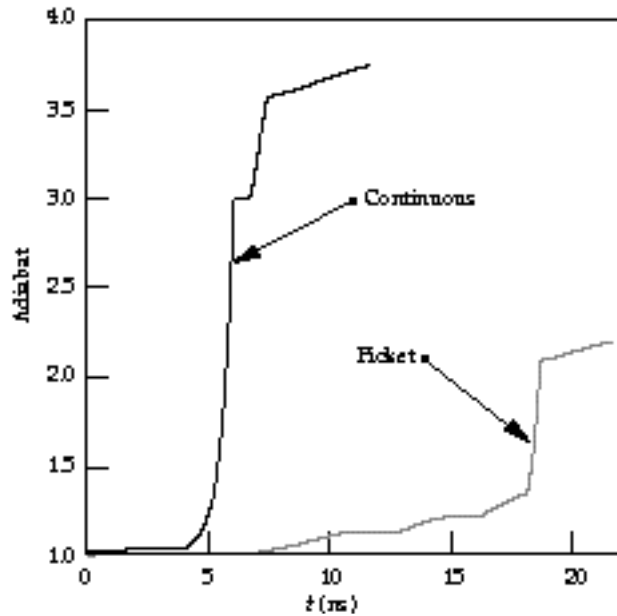


FIGURE 3. Fuel adiabat vs time for picket- and continuous-pulse capsules. (20-03-0397-0442pb01)

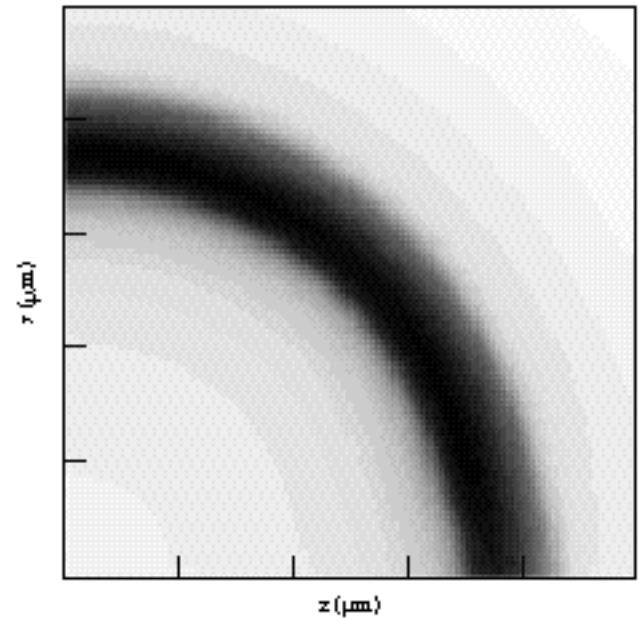


FIGURE 4. Gray scale indicates fuel density near ignition time in a 2D simulation of one quadrant of the continuous-pulse capsule design driven with the NIF beam geometry, assuming perfect pointing and power balance. (20-03-0397-0443pb01)

Illumination Uniformity

Direct- and indirect-drive capsules require uniformity over the capsule surface to a level of about 1% rms. For direct drive, this must be achieved by the laser. For indirect drive, x-ray transport between the capsule and the hohlraum wall effectively eliminates nonuniformity for approximately $l \geq 10$, while lower modes must be controlled by hohlraum geometry, beam pointing within the hohlraum, and beam phasing. For direct drive, nonuniformity in modes $l \leq 20$ is dominated by contributions from the beam geometry, pointing errors, power imbalance, and gross beam profile. Contributions for $l > 20$ are dominated by substructure within individual beams, which creates target modulations in a process called imprint, discussed later in this article.

2D simulations can examine implosion nonuniformity, resulting from the beam locations, by representing the laser illuminations as cones of beams. Only a full 3D simulation can examine a 3D structure resulting from discrete beams in each cone. Figure 4 shows fuel density at ignition time for a simulation of one quadrant of the continuous pulse design. Nonuniformities in the angular direction are small, and the simulation predicts full yield. We anticipate no significant nonuniformity in direct-drive implosions resulting from the beam configuration.

Beam pointing errors and power imbalance give additional irradiation nonuniformities. Figure 5 shows the level of nonuniformity expected for the pointing and power balance accuracy for which NIF has been

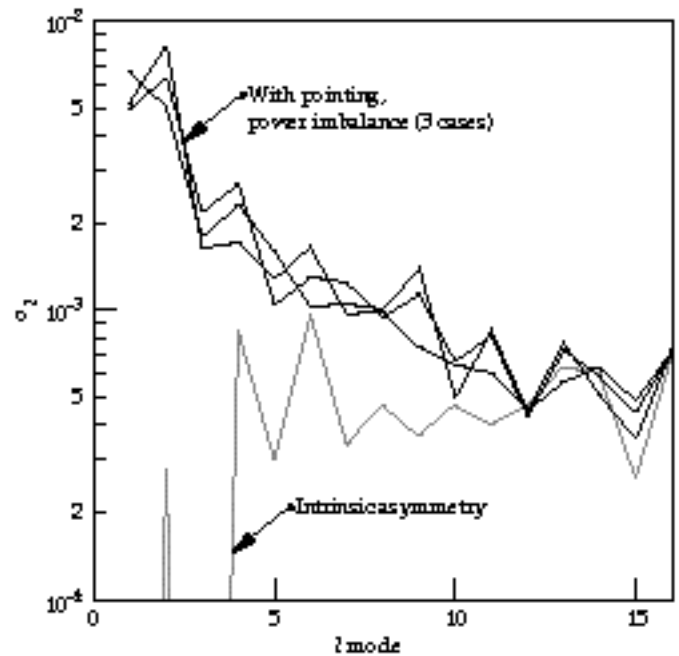


FIGURE 5. The solid lines show illumination nonuniformity (contribution of a given mode to the rms) vs spherical harmonic mode number l , for three random choices of pointing error and power imbalance consistent with NIF specifications. The shaded line shows intrinsic nonuniformity from the beam geometry alone. (20-03-0397-0444pb01)

designed—50 μm rms pointing accuracy for each beam cluster and 5% rms power imbalance for each beamlet.¹¹ These specifications follow the 1% rms illumination uniformity requirement. The white paper¹ gives the derivation of these laser specifications from the uniformity requirement. The nonuniformity has been calculated for three randomly selected sets of errors, and then broken down into spherical harmonic modes, Y_{lm} . The quadrature sum over m of the intensity rms, σ_l , is shown at each l mode. It may be seen that most of the nonuniformity is in modes $l = 1$ –4, and that the contribution from pointing errors and power imbalance dominates the intrinsic nonuniformity. At higher modes, the intrinsic component becomes a significant fraction of the total.

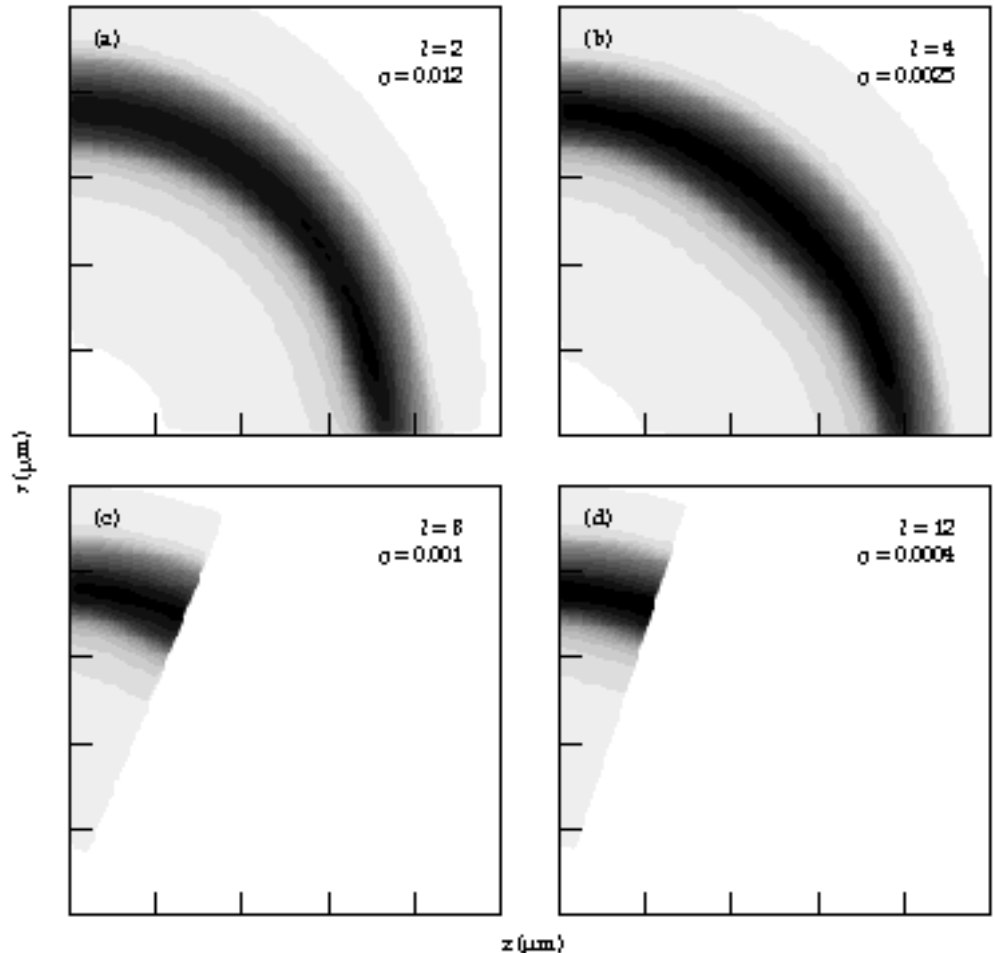
Drive nonuniformities from pointing deviations and power imbalance generally are not axisymmetric. To look at these effects in a 2D LASNEX simulation, we consider $m = 0$ for a single l mode at a time. Drive asymmetry is introduced as an angle-dependent energy deposition source, rather than the usual laser ray trace, as this gives better control of the spatial

structure and less numerical noise. Figure 6 shows results of simulations for $l = 2, 4, 8$, and 12 at levels comparable with the predicted values, none of which is very distorted. The capsule is subject to the sum of the distortions over l , which is several times worse than one of the single low l cases, but this should still be tolerable. Thus, the LASNEX simulations support the laser uniformity specifications in the white paper.

Laser Imprint

Illumination nonuniformity on smaller spatial scales, roughly $l > 20$, arises mainly from spatial modulation in individual beams. Imprint is the formation of target perturbations from small-scale intensity nonuniformity. Rayleigh–Taylor (RT) instability causes target perturbations in the range $20 < l < 200$ to grow by large factors during the implosion, so the uniformity must be very good. Beam smoothing is performed with random phase plates (RPPs)¹² and smoothing by spectral dispersion (SSD).¹³ RPPs break up the spatial coherence of the beam to give a laser spot with fine speckles

FIGURE 6. Fuel density near ignition time from simulations of single l mode drive asymmetry for (a) $\sigma_2 = 0.012$, (b) $\sigma_4 = 0.0025$, (c) $\sigma_8 = 0.001$, and (d) $\sigma_{12} = 0.0004$. A full quadrant was simulated for $l = 2, 4$, while $l = 8, 12$ were modeled with a wedge between the first peak and valley of the modulation. (20-03-0397-0445pb01)



and a smooth envelope. The RPP spot has a total modulation $\sigma_{\text{rms}}/I_0 = 1$, where I_0 is the mean intensity, and there is power on all spatial scales larger than the speckle size. SSD reduces the modulation further by introducing bandwidth to the laser beam and dispersing the spectral components with a grating, giving a different speckle pattern every coherence time so that the spot is smoothed in the time average. To get the smoothing level needed for direct drive, $\sigma_{\text{rms}}/I_0 < 0.01$, the beam must be dispersed in both directions, which is called 2D SSD. While 1D SSD may help mitigate laser-plasma instabilities for indirect drive, we believe that 2D SSD is needed to meet the more stringent requirements of direct drive. At best, the modulation is reduced to $\sigma_{\text{rms}}/I_0 = (t_c/t_{\text{avg}})^{1/2}$, where t_c is the coherence time, related to the bandwidth $\Delta\nu$ by $t_c = 1/\Delta\nu$, and t_{avg} is the averaging time. A more detailed description of the effects of the beam smoothing parameters upon the character of the intensity nonuniformity has been presented elsewhere.¹⁴

We simulated imprint by calculating the target modulation introduced by single-mode time-independent intensity modulations. The structure of a perturbation resulting from laser speckle is found to become indistinguishable from that of a perturbation that started out as a surface bump after some characteristic relaxation time.^{15,16} The relaxation time is often the beginning of bulk acceleration of the shell, when perturbations of any origin relax into eigenmodes of the RT instability. Also, the amplitude of the target perturbation is proportional to the size of the intensity modulation. Therefore, it is convenient to relate the imprinted perturbation to a surface finish perturbation that develops into the same size structure after the relaxation time, called the equivalent surface finish, ϵ_l . Then, we scale out the intensity modulation to get a quantity called the imprint efficiency, $E_l = \epsilon_l/(\delta I_l/I_0)$, where δI_l is the intensity modulation amplitude in mode l . Figure 7 shows the imprint efficiency calculated for several mode numbers. These simulations were conducted in planar geometry, as convergence effects are small during the imprint timescale, and used a modulated energy deposition source, as described earlier.

Imprint is generally effective for only a limited period of time—intensity nonuniformity has less effect upon a target at later times. One reason is that heat conduction gives thermal smoothing¹⁷ between where the laser energy is absorbed and the ablation front. Modulation of ablation pressure is predicted to be reduced from the modulation in laser intensity as $\delta P/P = e^{-k\Delta r}$, where δP is the ablation pressure modulation, k is the wave number of the transverse intensity modulation, and Δr is the separation between where the laser energy is deposited and the ablation front. Thermal smoothing is greater for shorter wavelengths or higher mode

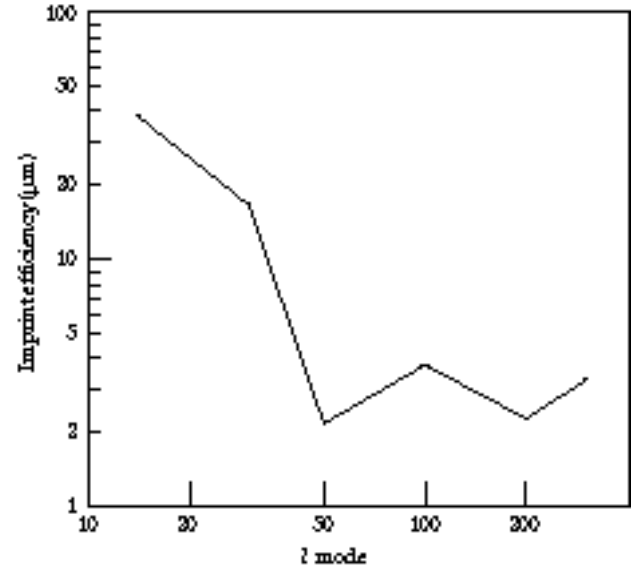


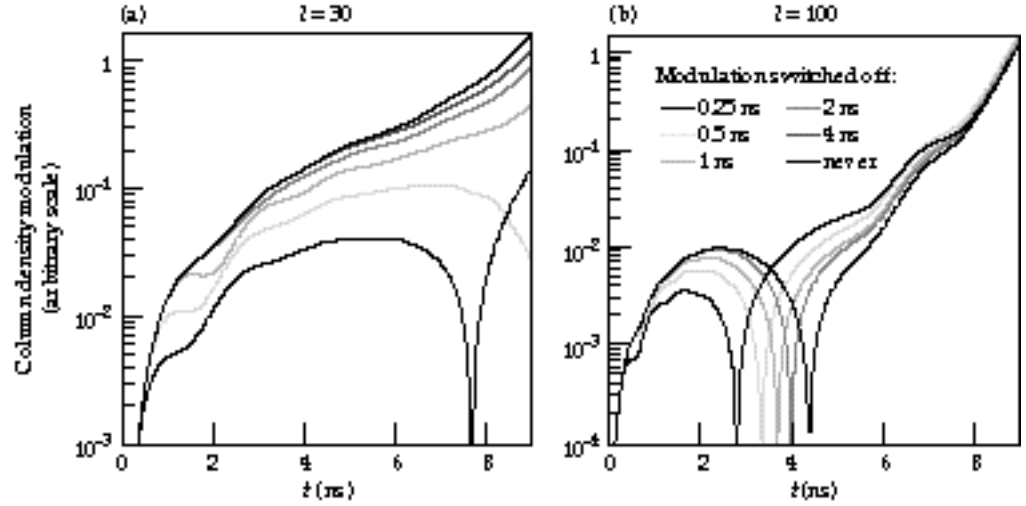
FIGURE 7. Imprint efficiency vs spherical harmonic mode number for the continuous-pulse NIF design. (20-03-0397-0433pb01)

numbers and increases with the thickness of the ablated plasma. Also, once hydrodynamic perturbations are created at the ablation front, they grow by the RT and Richtmyer–Meshkov (RM) instabilities. Over time, additional imprint becomes less and less significant compared with earlier imprint, which has been amplified by growth. Note that the imprint time may not be the same as the relaxation time. Imprint may have terminated before the shell begins bulk acceleration, but the longitudinal structure of the imprinted perturbation may differ from that of a surface finish perturbation until both relax into an RT eigenmode.

A timescale over which imprint occurs has been examined with simulations in which the intensity pattern is switched from modulated to spatially uniform at different times. Figure 8 shows column density modulation, taken from planar simulations of modulation wavelength corresponding to $l = 30$ and $l = 100$, for cases in which the laser was made spatially uniform after 0.25, 0.5, 1, 2, or 4 ns. The later we switch to uniform illumination, the closer the results are to these with constant modulation. We can extract a characteristic time by which 80% of the imprint has occurred (about 1.4 ns for $l = 100$ and 4.9 ns for $l = 30$). Phase oscillations somewhat complicate interpretation of the imprint timescale, especially for the $l = 100$ case.

An equivalent surface finish modal spectrum was obtained by multiplying the imprint efficiency by the predicted spectrum of optical modulation, using a simplified smoothing model in which an independent speckle pattern is generated every laser coherence time. (Reference 14 provides a more complete model.) We took the imprint timescale to be 2 ns, independent of l , and the coherence

FIGURE 8. Column density modulation amplitude from imprint simulations for (a) $l = 30$ and (b) $l = 100$. The heavy solid line shows the case where the intensity is modulated at all times, while the shaded curves show cases in which the laser is made spatially uniform at various times. (20-03-0397-0434pb01)



time to be 2 ps, from the NIF direct-drive bandwidth of 0.5 THz. Overlap of 50 beamlets and two polarizations at any spot on the capsule gives an additional smoothing factor of 10. The equivalent surface finish spectrum, shown in Figure 9, is comparable in amplitude with the surface finish from fabrication measured for Nova capsules.¹⁸ The rms modulation from imprint is 11 nm and that from fabrication is 8.4 nm, adding in quadrature to a total effective surface finish of 13.9 nm. These spectra do not include a rise in the fabrication spectrum at low mode

numbers ($l < 16$), neglected in the fit shown here, or intensity modulation in low modes due to beam pointing and power imbalance.

The bandwidth and divergence requirements for beam smoothing stress the laser performance in some respects. Frequency-conversion efficiency decreases with increasing bandwidth, although this effect can be mitigated to some degree with, for example, three crystal conversion schemes. Spatial filter pinhole closure can limit the divergence. Since imprint occurs mainly during the early, low-power phase of the pulse, it seems likely that smoothing requirements at peak power should be less stringent. The beam smoothing specifications in the white paper¹ assume that the bandwidth requirement at peak power can be relaxed a factor of two below that for the foot of the pulse. Further research is needed to refine this estimate.

Ablation Front Perturbation Growth

Growth at the ablation front of perturbations initiated either by imprint or surface finish may be evaluated using the dispersion relation for ablative RT^{19,20}

$$\gamma_k = \sqrt{\frac{gk}{1+kL}} - 3kv_a, \quad (1)$$

where γ_k is the growth rate at wave number k , the acceleration $g = 8.5 \times 10^{15} \text{ cm/s}^2$, the density gradient scale height $L = 0.5 \text{ } \mu\text{m}$, and the ablation velocity $v_a = 3.4 \times 10^5 \text{ cm/s}$. Numerical values are averages over the shell acceleration from a 1D simulation of an implosion. The wave number is related to the mode number by $k = l/r$, where we use $r = 0.1 \text{ cm}$ as

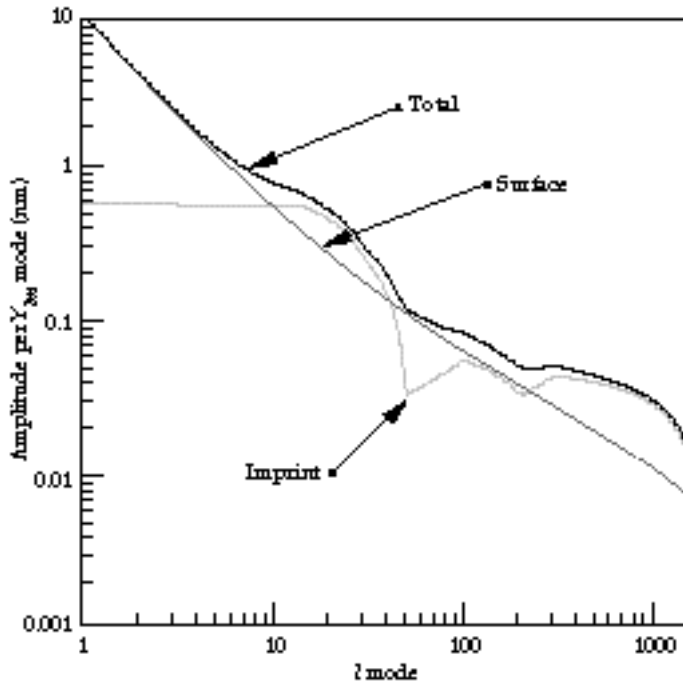


FIGURE 9. Amplitude per spherical harmonic mode number Y_{lm} vs mode number l for imprint modulation expressed as equivalent surface finish, actual surface finish, and total effective initial surface modulation. (20-03-0397-0435pb01)

a mean shell radius for this time interval. LASNEX simulations of linear regime mode growth have been used to check that this dispersion relation is applicable. The peak growth rate is about 2 ns^{-1} at $l \approx 150$. The total linear growth factor to the time of peak inward velocity is

$$GF_{\text{abl}}(k) = e^{\gamma_k \Delta t}, \quad (2)$$

where $\Delta t = 4.66 \text{ ns}$ is the acceleration time. Figure 10 shows the ablation front growth factors from Eq. (1) for the continuous pulse capsule design and for an $\alpha \approx 1$ design. It is clear that raising the adiabat improves stability. The ablation velocity is defined as $v_a = \dot{m} / \rho_{\text{max}}$, where \dot{m} is the mass ablation rate and ρ_{max} is the peak density in the shell. The mass ablation rate changes little if the shell adiabat is changed while the laser intensity is held fixed. However, for a given ablation pressure, $\rho_{\text{max}} \propto \alpha^{-3/5}$, so a higher α gives a higher v_a , thus more stabilization. The GF_{abl} curve for the $\alpha = 1$ design uses $L = 0.3 \mu\text{m}$ and $v_a = 1.8 \times 10^5 \text{ cm/s}$, with other parameters the same. This gives a peak GF_{abl} that is larger by more than 10^3 than for the higher adiabat design, while the GF_{abl} for $l = 100$ is larger by a factor of about 10.

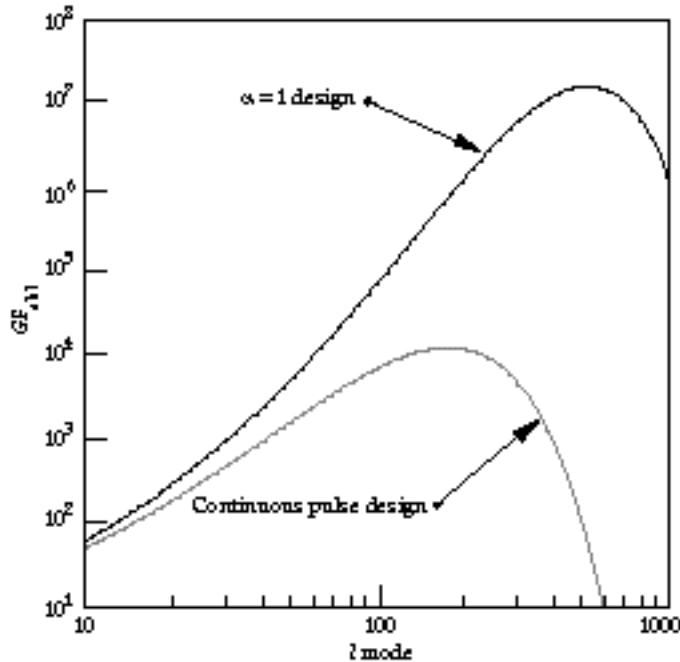


FIGURE 10. Growth factor for ablation front perturbations during inward acceleration vs mode number l from the dispersion relation Eq. (1), for the continuous-pulse capsule design, and for an $\alpha = 1$ design. (20-03-0397-0436pb01)

The modal amplitudes for linear growth were obtained by multiplying the effective surface finish spectrum by the growth factors. Figure 11 shows the ablation front perturbation spectrum at peak shell velocity. According to the multimode saturation theory of Haan,²¹ modes with amplitudes greater than vr/l will be affected by saturation. We used $v = 2$ for the saturation parameter.²² Modes near the peak of the linear growth spectrum are substantially affected by saturation. After saturation effects are considered, the peak in the amplitude spectrum is shifted down to $l \approx 60$. The total rms amplitude of RT bubbles obtained from this spectrum is $6.4 \mu\text{m}$, well under the total shell thickness (to $1/e$ of peak density) at peak velocity of $135 \mu\text{m}$. The rms bubble amplitude for the $\alpha = 1$ design is $30 \mu\text{m}$ with saturation effects included in the same manner, although the rms, based upon linear growth factors, is 5 cm . The total shell thickness at peak velocity is $91 \mu\text{m}$ for the low adiabat design, but as the peak amplitude is several times the rms, the shell would be penetrated.

The Haan saturation model does not include addition of power to modes through multimode coupling.²³ The high degree of saturation for the most rapidly growing modes in this case causes concern that a turbulent cascade could feed more power into the lower l modes than was obtained by the analysis above, which assumed only growth from the seed amplitude of each individual l .

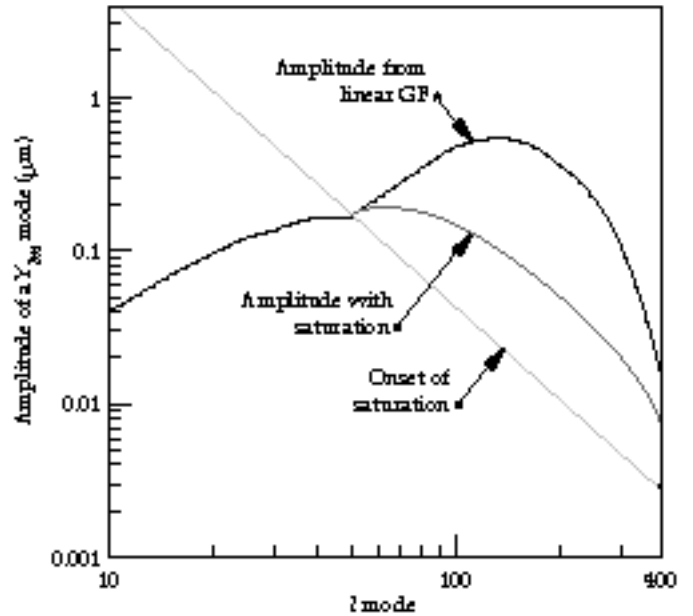


FIGURE 11. Ablation front modulation amplitude at peak velocity vs l mode from linear growth factors, corrected for saturation, and amplitude for onset of saturation. (20-03-0397-0437pb01)

mode. To address this issue, we used a 2D multimode simulation using finite modal amplitudes, including modes in the range $10 \leq l \leq 200$ in a wedge of a sphere extending from $\theta = \pi/2$ out to the first minimum of the P_{10} Legendre polynomial. The modes were represented as *cosine* harmonics of the lowest mode. Although these modes differ slightly from *spherical* harmonics, as the latter do not match a single reflection boundary in a wedge, the difference should have little effect on the results. The mode amplitudes were adjusted so that the total power in all Y_{lm} , $10 \leq l \leq 200$ was included in the reduced set of modes ($l = 10, 20, \dots, 200; m = 0$) included in the simulation. We simulated imprint of static speckle with an amplitude corresponding to a 2-ns time-average for the beam smoothing conditions described earlier. The true averaging time varies with mode number, but it is probably within a factor of two of this value for the important modes, so these amplitudes should be accurate to within a factor of $\sqrt{2}$. No surface finish modulation was included in this simulation.

Figure 12 compares the rms modulation of the ablation front radius postprocessed from the 2D multimode simulation with two applications of the Haan quasilinear analysis. One Haan application uses the growth factors from the dispersion relation in Eq. (1) applied to perturbations arising from imprint alone. The other uses linear growth factors from 2D LASNEX single-mode simulations. All three cases agree to within a factor of about two. The Haan application with LASNEX

growth factors should agree identically with the multimode simulation when the perturbations are linear. However, there is some disagreement because the evolution of every included mode was followed in the multimode simulation, while the Haan model application interpolated between a smaller number of discrete l values, which were actually simulated. The multimode simulation shows that the Haan theory gives a reasonably good result even though linear growth factors for this case predict a high degree of saturation.

The Haan theory may be applied to perturbation amplitudes at the inside of the shell as well, where perturbations can feed through from the ablation front, grow during deceleration of the shell, and penetrate into the hot spot that ignites the capsule. Figure 13 shows linear growth factors to the inner surface, defined as the ratio of amplitude at the hot spot boundary at ignition to initial outer surface amplitude. The model for shell feedthrough at deceleration growth is very simplified. The feedthrough factor is $F_{ft} = (1 + 1/\eta)^{-l}$, where $\eta = r/\Delta r = 16$ is an average shell aspect ratio. As much of the deceleration is from a single strong shock, we used for the deceleration growth factor the RM instability expression $GF_d = 1 + \Delta v k A$, where the velocity change $\Delta v = 3.8 \times 10^7$ cm/s, the Atwood number $A = 0.5$, and a radius of $150 \mu\text{m}$ is used to obtain the mode number k from l . The total linear growth factor to the hot spot boundary is $GF_{hs} = GF_{abl} \times F_{ft} \times GF_d$. Note that the peak GF_{hs} is

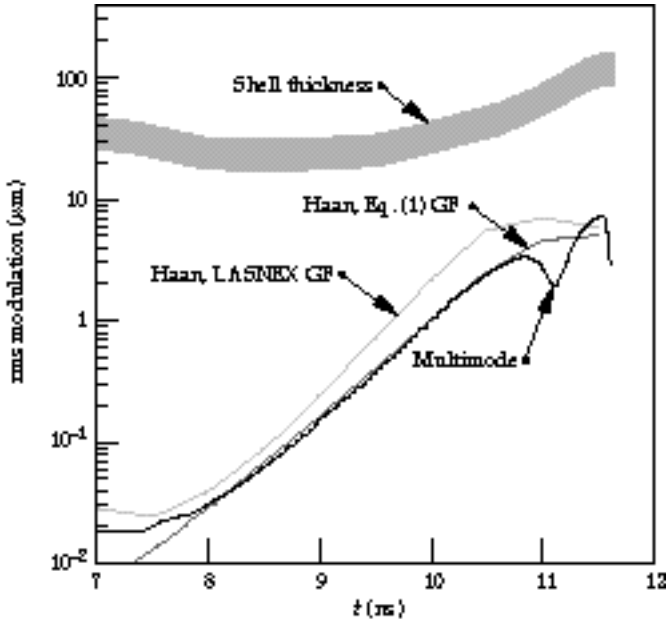


FIGURE 12. Ablation front rms modulation amplitude vs time postprocessed from a LASNEX 2D multimode simulation, from application of the Haan model using linear growth factors from Eq. (1), and from the Haan model using LASNEX single-mode simulations. The approximate shell thickness is also shown. (20-03-0397-0438pb01)

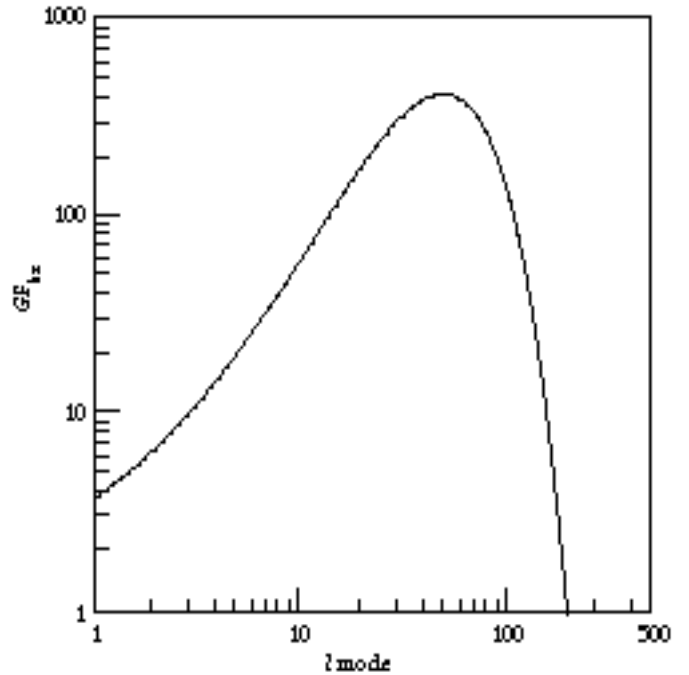


FIGURE 13. Hot spot growth factor vs mode number. The hot spot linear growth factor is the ratio of the amplitude on the outside of the hot spot at ignition time to the initial outer surface amplitude. (20-03-0397-0439pb01)

approximately equal to 400 at $l \approx 50$, which is smaller than the peak GF_{abl} and peaks at a lower l , because the high modes feed through inefficiently.

Penetration of cold fuel into the hot spot at ignition time was assessed similarly to ablation front penetration. The outer surface initial amplitude spectrum from Figure 9 was multiplied by GF_{hs} ; then, saturation effects were applied using the Haan model. Figure 14 shows the resulting hot spot amplitude spectrum. The degree of nonlinearity at the hot spot boundary is more moderate than was the case at the ablation front. The rms bubble amplitude with saturation effects is predicted to be $3.7 \mu\text{m}$, while the amplitude resulting from linear growth factors would be $9.6 \mu\text{m}$. The spike amplitude, which is 1.5 times larger, is about 10% of the hot spot radius. This analysis predicts that penetration into the hot spot is not great enough to impede ignition or to significantly reduce the capsule yield. We have not yet examined sensitivity to the DT ice roughness, which we assume to be similar to that for indirect drive.

Conclusions

We have examined direct-drive capsule designs that could achieve ignition in NIF. Beam geometry suitable for imploding direct-drive capsules will be provided by steering some of the beams from the indirect-drive configuration to an additional pair of rings near the waist of the chamber. Achievable beam pointing accuracy and power balance is predicted to give satisfactory uniformity to the implosions. Simulations of laser imprint have been

used to set the beam smoothing requirements for direct drive. A laser bandwidth of 0.5 THz on the foot of the pulse is predicted to cause target perturbations comparable with those from a surface finish of $\sim 10 \text{ nm}$.

RT growth factors at the ablation front reach several thousand for these designs, which have been tuned to a fuel adiabat of $\alpha = 3-4$, and growth factors for a low adiabat design are much larger. Ablation front modulations for the nominal design are predicted to become substantially nonlinear by peak shell velocity, but when saturation effects are included, the shell is predicted to remain intact. Multimode simulations confirm predictions of the Haan model on the effects of saturation. Similar analysis at the hot spot boundary predicts penetration of about 10% of the hot spot radius. These results give us a basis for believing that ignition can be achieved.

Notes and References

1. D. Eimerl, Ed., "Configuring the National Ignition Facility for Direct-Drive Experiments," Lawrence Livermore National Laboratory, Livermore, CA, UCRL-ID-120758 (1995).
2. R. Sawicki, Ed., "Advanced Conceptual Design Review," Lawrence Livermore National Laboratory, Livermore, CA, NIF-LLNL-96-065, internal document (1996).
3. S. W. Haan et al., *ICF Quarterly Report* 5(4), 215-225, Lawrence Livermore National Laboratory, Livermore, CA, UCRL-LR-105820-95-4 (1995).
4. J. Meyer-ter-Vehn, *Nucl. Fusion* 22, 561-565 (1982).
5. J. Lindl, *Phys. Fluids* 2(11), 3933-4024 (1995).
6. J. D. Lindl and J. D. Kilkenny, *ICF Quarterly Report* 5(4), 209-214, Lawrence Livermore National Laboratory, Livermore, CA, UCRL-LR-105820-95-4 (1995).
7. T. R. Boehly et al., *Rev. Sci. Instrum.* 66, 508 (1995).
8. J. D. Sethian et al., *Fusion Technology* 26(3), 717-721 (1994).
9. C. Yamanaka et al., *J. Quantum Electron.* QE-23, 1361 (1987).
10. C. P. Verdon, *Bull. Am. Phys. Soc.* 38, 2010 (1993).
11. S. M. Pollaine and D. Eimerl, "Modal Analysis of Directly Driven ICF Targets," Lawrence Livermore National Laboratory, Livermore, CA, UCRL-JC-125731; submitted to *Nucl. Fusion Lett.* (1997).
12. Y. Kato, K. Mima, N. Miyanaga, S. Aringa, et al., *Phys. Rev. Lett.* 53, 1057 (1984).
13. S. Skupsky et al., *J. Appl. Phys.* 66, 3456 (1989).
14. J. E. Rothenberg, *Proc. Soc. Photo-Opt. Instrum. Eng.* 2633, 634 (1995).
15. S. G. Glendinning et al., *Phys. Rev. E*, 54, 4473 (1996).
16. S. V. Weber et al., "Simulations of Laser Imprint for Nova Experiments and for Ignition Capsules," Lawrence Livermore National Laboratory, Livermore, CA, UCRL-JC-124547; *Phys. Plasmas* 4, 1978 (1997).
17. S. E. Bodner, *J. Fusion Energy* 1, 221 (1981).
18. R. McEachern et al., *ICF Quarterly Report* 4(1), 25-30, Lawrence Livermore National Laboratory, Livermore, CA, UCRL-LR-105820-94-1 (1994).
19. H. Takabe, L. Montierth, and R. L. Morse, *Phys. Fluids* 26, 2299 (1983); H. Takabe, K. Mima, L. Montierth, and R. L. Morse, *ibid.* 28, 3676 (1985).
20. J. Lindl, *Phys. Plasmas* 2, 3933 (1995).
21. S. W. Haan, *Phys. Rev. A* 39, 5812 (1989).
22. M. J. Dunning and S. W. Haan, *Phys. Plasmas* 2, 1669, (1995).
23. S. W. Haan, *Phys. Fluids B* 3, 2349 (1991).

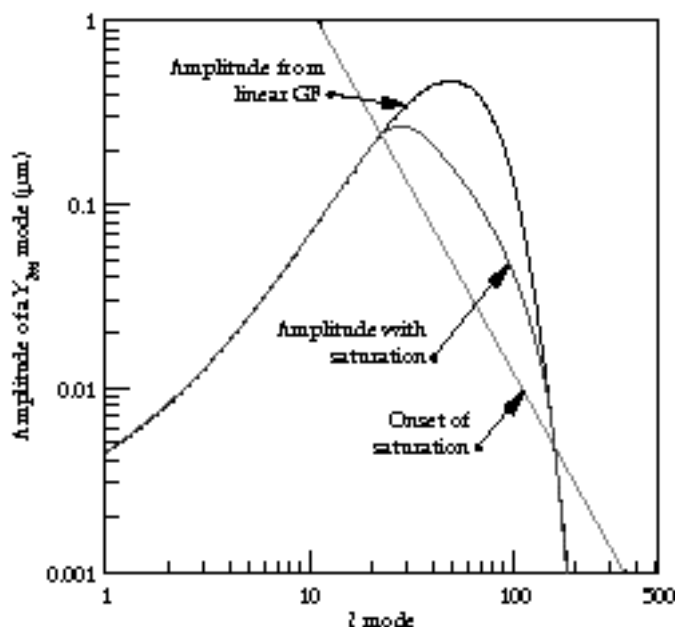


FIGURE 14. Modulation amplitude at the hot spot boundary at ignition time vs l mode from linear growth factors, corrected for saturation, and amplitude for onset of saturation. (20-03-0397-0440pb01)